

A method for monitoring glacier mass balance using satellite albedo measurements: application to Vatnajökull, Iceland

MARTIJN S. DE RUYTER DE WILDT,¹ JOHANNES OERLEMANS,¹ HELGI BJÖRNSSON²

¹*Instituut voor Marien en Atmosferisch Onderzoek, Universiteit Utrecht, Princetonplein 5, 3584 CC Utrecht, The Netherlands*

E-mail: wildt@phys.uu.nl

²*Science Institute, University of Iceland, Dunhaga 3, IS-107 Reykjavík, Iceland*

ABSTRACT. We compare satellite albedo images of Vatnajökull, Iceland, with mass-balance measurements for the years 1991–99. We find that the equilibrium line is mostly not visible when it is located above its position of the previous year(s). Equilibrium-line detection is further hindered by clouds and a gradual transition between ice and firn or snow. Consequently, firn-line elevation at the end of the melting season is not particularly useful for estimating the annual mass balance. Instead, we propose to study the mean albedo of the entire ice cap throughout the melting season so that all available information about the surface albedo is taken into account. The mean net potential global radiation, which can be estimated from the mean surface albedo alone, both depends on and influences summer melt. It also depends on winter precipitation and, integrated over the melting season, is found to relate linearly to the specific mass balance B ($r = 0.87$ and 0.94 for different outlets of Vatnajökull). B can be estimated quantitatively when this relation is known and qualitatively when it is not. The uncertainty in the satellite-derived value of B is 0.5 – 0.8 m w.e., which for Vatnajökull corresponds to about 27% of the interannual variability of B .

1. INTRODUCTION

In recent years there has been significant interest in the state of the cryosphere, because of its sensitivity to climate change. Changes in the cryosphere influence sea level and local climate and are good indicators of climate change. Large parts of the cryosphere, however, lie in remote areas. In only a few places have quantities such as mass balance and terminus location been measured with sufficient temporal and spatial resolution. Satellite remote sensing is a valuable tool for overcoming this problem; it can be used to observe large parts of the cryosphere on a regular basis without the need to actually go there. Decadal-scale changes in the extent of glaciers and ice caps have been monitored with Landsat reflectance images (e.g. Hall and others, 1992; Hastenrath and Greischar, 1997; Williams and others, 1997). It is less straightforward, on the other hand, to detect yearly variations in mass-balance components. Satellite passive-microwave sensors can possibly detect the amount of accumulation (Zwally, 1977), although only over regions with dry snow and with little accumulation, and the amount of hoar formation also needs to be known (Abdalati and Steffen, 1998). As a consequence, this method has not yet been used in practice. Microwave data can also reveal the boundary between dry and wet snow, which is why they have also been used to measure the spatial extent (but not the amount) of surface melt (e.g. Steffen and others, 1993; Mote and Anderson, 1995).

A quantity often found to relate linearly to the mean specific mass balance (B) is the equilibrium-line altitude (ELA) (e.g. Østrem, 1975; Hagen and Liestøl, 1990). According to Østrem (1975), this relation can be used to determine B from satellite images that are taken close to the end of the melting

season, provided that the boundary between snow and firn (i.e. the equilibrium line) can be detected. Note that we define firn as all snow that is at least 1 year old, to distinguish it from snow that fell in the mass-balance year under consideration. This method has been applied by several authors (e.g. Pelto, 1987; Kulkarni, 1992), although only a few actually validated the satellite-derived mass balance with ground measurements (e.g. Rott and Markl, 1989; Demuth and Pietroniro, 1999). There are several reasons for this. First of all, continuous mass-balance records that can be coupled to satellite-derived glacier properties exist for only a few glaciers. Furthermore, satellite reflectance images often clearly show the boundary between ice and firn or snow (e.g. Williams, 1987; Reijmer and others, 1999), but snowfall near the end of the melting season can suddenly lower the snowline and hence obscure the equilibrium line. When superimposed ice is present, the equilibrium line lies below the snowline. Apart from this, clouds often limit the availability of reflectance images. Clouds do not pose a problem when radar images are used. The transient snowline is detectable on radar images (e.g. Rott and Mätzler, 1987; Adam and others, 1997; Smith and others, 1997; Brown and others, 1999), but in these studies it has not been related to the ELA or to B . Although these studies show that the firn line at the end of the melting season can be detected, this does not automatically mean that B can be inferred. The snowline, corresponding to the equilibrium line, is clearly visible when no firn is exposed (Fig. 1a). In the other case, the equilibrium line lies above the firn line (Fig. 1b) and may not be detectable due to small albedo differences between firn and snow a few weeks or months old. This has been observed by Rott and Markl (1989) and more recently by Hall and others (2000) and König and others (2001).

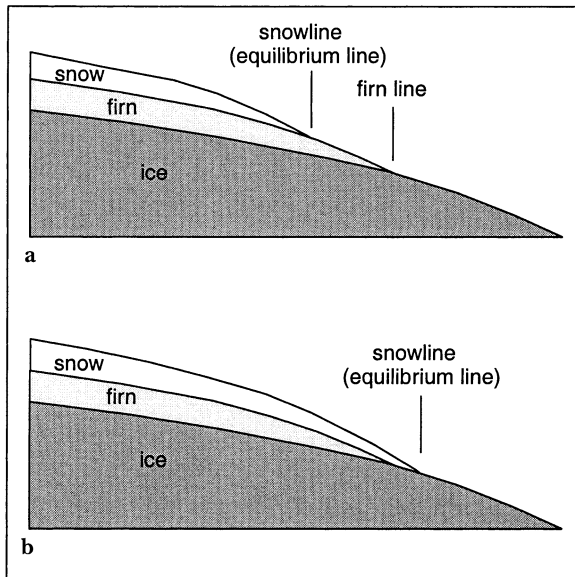


Fig. 1. Glacier-facies classification for the end of the melting season, based on the age of the material. Superimposed ice is not shown, because in Iceland it is only found sporadically. (a) When the mass balance is much more negative than in previous years, firn is exposed and the equilibrium line lies above the firn line (after Brown and others, 1999). (b) In the opposite case, when snow covers all firn, only the equilibrium line and not the firn line is visible.

Demuth and Pietroniro (1999) used the known relation between the ELA and B for Peyto Glacier, Canada, to determine B from the satellite-derived snowline position. However, they did this for one year which displayed a lower ELA than previous years. Furthermore, they noted that digital elevation model (DEM) and satellite image resolution can limit the detection of changes in ELA. Rott and Markl (1989) used images from a year with positive B and from a year with negative B . They could delineate the snowline in the year

with negative B on Hintereisferner, Austria, but not on neighbouring Kesselwandferner. Another study in which satellite observations are quantitatively coupled to mass-balance observations is from Greuell and Knap (2000). For a period of 8 years, these authors find a correlation between the satellite-derived slush-line position and B for the Greenland ice sheet, but the applicability of this relation is limited because of an upper boundary which the slush line cannot exceed.

In this paper, we use mass-balance data and satellite images from several years to analyze the relation between the firn line and the equilibrium line. We also describe a new method to infer B from satellite images, which only requires satellite imagery. This means that it can be applied to any ice cap or glacier. An important aspect of the method is that the whole surface of a drainage basin during the melting season is studied, and not only a specific transition between glacier facies for a specific day. This takes into account all available information about the surface albedo. As a test case we study Vatnajökull, Iceland. For this ice cap there are mass-balance measurements available, with which the satellite images can be compared quantitatively. Vatnajökull is one of the largest temperate ice masses in the world (8200 km² in 1995) and consists of several domes, large lobes and valley glaciers (Fig. 2). Owing to the position of Iceland in the middle of the North Atlantic storm track, the skies are overcast most of the time, and albedo retrieval is often not possible. This means, however, that if we can use satellite albedo images to retrieve B here, cloudiness will probably not be a problem for ice masses that are less frequently covered by clouds. Because of the size of Vatnajökull, Advanced Very High Resolution Radiometer (AVHRR) images from the U.S. National Oceanic and Atmospheric Administration (NOAA) satellites, which have a resolution of 1.1 km at nadir, can be used. These images are not expensive and have the advantage of being available several times per day, so obtaining good time series is feasible. Both in situ data and satellite data are from the years 1991–99 inclusive.

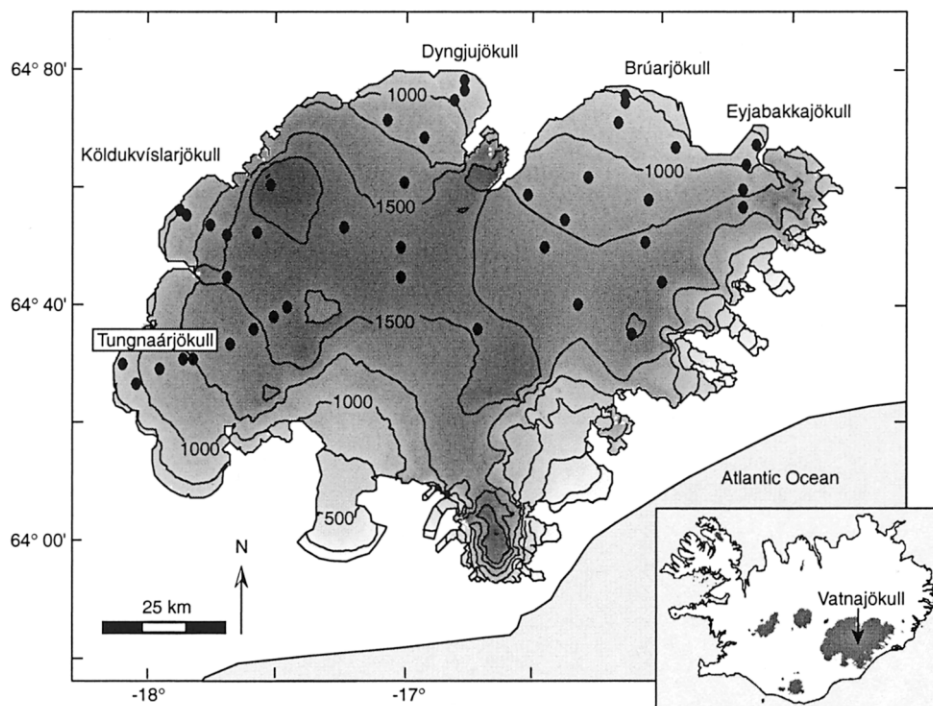


Fig. 2. Map of Vatnajökull, based on the DEM used for image processing. The DEM has a horizontal resolution of 500 m. Height contours are shown for each 250 m interval. Indicated are the outlets where the mass balance has been regularly measured. The black circles indicate sites where the mass balance has been measured.

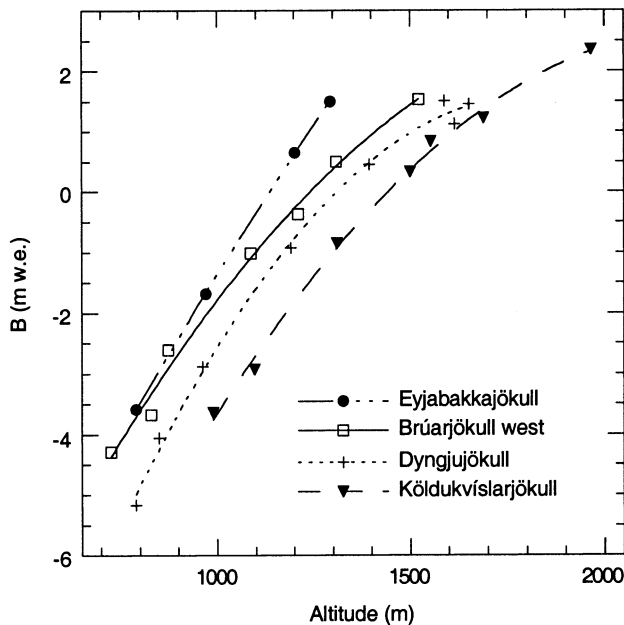


Fig. 3. Average mass-balance gradient along the flowlines of four representative drainage basins of Vatnajökull. Each point represents a measurement site. The curve fits are second-order polynomials.

2. IN SITU MASS-BALANCE DATA

The mass balance of Vatnajökull has been measured with sufficient spatial resolution since 1992 (Björnsson and others, 1997, 1998a, b, c, 1999; Sigurdsson, 1997; personal communication from O. Sigurdsson, 2001). For one drainage basin (Eyjabakkajökull), data from 1991 are available. The data have mainly been obtained over the drainage basins of Eyjabakka-, Brúar-, Dyngju-, Köldukvíslar- and Tungnaárjökull (Fig. 2). Most measurements were taken at the end of September or the beginning of October. On each outlet, the mass balance has been measured along one or two profiles which capture the altitudinal variation. Figure 3 displays the mass-balance gradient for some drainage basins. It shows that the amount of annual precipitation influences the mean ELA: the ELA varies from about 1050 m (Eyjabakkajökull) to about 1440 m (Köldukvíslarjökull). Eyjabakkajökull lies closest to the coast and receives most precipitation, while Köldukvíslarjökull has a less maritime and drier climate. Because most of Vatnajökull is quite flat, the profiles can be used together with a few additional meas-

urement sites to describe the lateral variation. The mean specific balances of the areas are obtained by interpolation between the measurement sites. For this interpolation, we developed an algorithm that takes into account vertical gradients. A DEM is needed for this feature to work. For each gridpoint of the DEM (displayed in Fig. 2), the algorithm determines the n closest measurement sites within 500 m in altitude from the gridpoint. Then, because of the limited height differences, a linear relation between mass balance and altitude is found for the n measurement sites, with which the mass balance at the gridpoint can be calculated. To smooth discontinuities in the resulting mass-balance field, the contribution of each measurement site is weighted with the inverse of its distance to the gridpoint. The resulting values of B are not very sensitive to the value of n . We therefore use a value of 6, which is the lowest value that gives smooth mass-balance fields. The resulting mean specific mass balances are displayed in Table 1. The data clearly include years with a highly positive B (1992, 1993) and years with a highly negative B (1997, 1998).

3. SATELLITE IMAGES: PROCESSING

AVHRR images were purchased from the Satellite Receiving Station at the University of Dundee, Scotland. We selected 107 images taken from April until September that display few clouds over the ice cap (9–15 images per year). Images from the years 1991–94 were taken from the NOAA-II satellite. Afterwards, the NOAA-14 satellite provided the images. The images cover the melting seasons of most years reasonably well. For 1993, which had a cold summer with high cloudiness, we found the fewest images (9), and only two images that had been taken before 15 July. Most images display clouds, so on a certain image some drainage basins may be largely covered by clouds. Nearly all images were taken close to solar noon so that solar irradiance was large. The solar zenith angle ranged between 40° and 66° on all images, except for one at the very beginning of the melting season. The satellite images need to be processed in order to retrieve the surface albedo. The retrieval method is based on the method of Reijmer and others (1999), although there are a few differences. The processing steps are described below and include cloud masking, geolocation, calibration, atmospheric correction, narrow- to broadband conversion, correction for anisotropy of the reflected radiation and correction for surface inclination.

Table 1. Mean specific mass balances (in m w.e.) as obtained by interpolation for different drainage basins of Vatnajökull. The weighted mean for the whole northwestern part of Vatnajökull ('All') is shown when the mass balance was measured over the largest part of this area. The bottom row displays the means and the standard deviation of each time series

Year	Western Brúarjökull	Eastern Brúarjökull	Eyjabakkajökull	Dyngjujökull	Köldukvíslarjökull	Tungnaárjökull	All
1991			-0.9				
1992					0.81	0.35	
1993	1.32	0.89	0.69	1.58		0.23	1.16
1994	0.55		0.42	0.36	0.03	-0.11	0.31
1995	0.22		-0.48	0.04	-0.64		-0.31
1996	-0.04	-0.76	-0.88	-0.21	-0.68		-0.54
1997	-1.04	-1.79	-1.88	-0.85	-1.07	-2.18	-1.3
1998	-0.46	-0.94	-1.57	-0.53	-0.8	-1.53	-0.77
1999	-0.09	-0.56	-0.72		-0.58	-0.99	-0.26
Mean	0.07 ± 0.28	-0.63 ± 0.43	-0.66 ± 0.31	0.07 ± 0.35	-0.42 ± 0.24	-0.71 ± 0.42	-0.24 ± 0.30

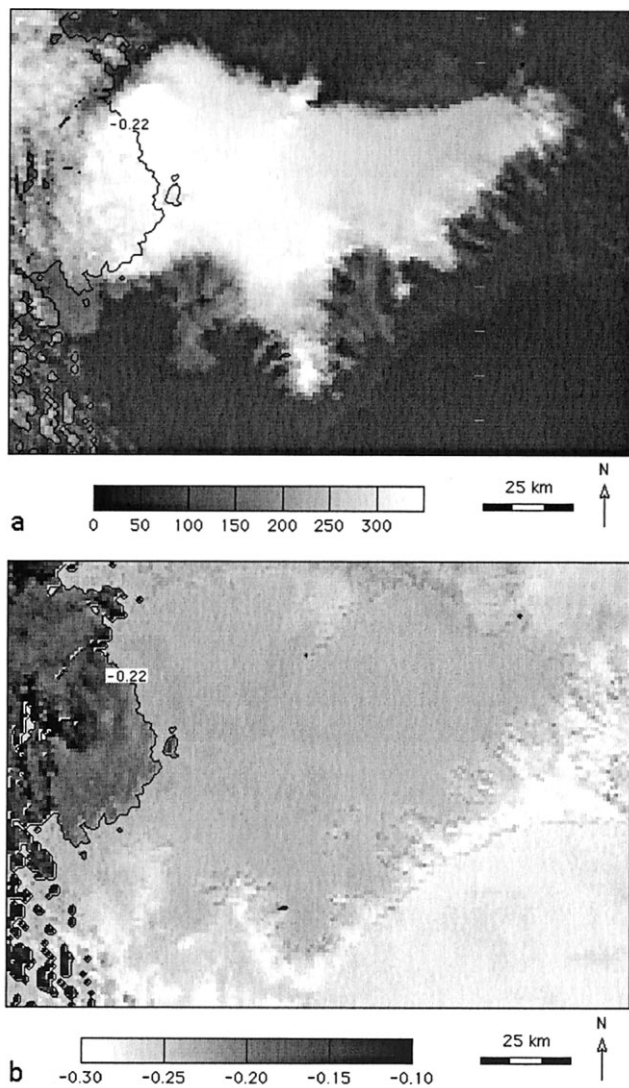


Fig. 4. Channel 1 count number (a) and normalized differential cloud index (b) for Vatnajökull on 8 September 1996. In both plots the -0.22 contour of the normalized differential cloud index is shown.

3.1. Cloud masking

Developing fully automated techniques for cloud masking over snow surfaces is difficult, because clouds can have the same thermal and visible characteristics as snow. There are automated techniques that detect textural characteristics of clouds (Ebert, 1987), but these could not be applied to Vatnajökull because they classify some of the glacier's surface as clouds (e.g. bands of low ice albedo, firn-ice transition). Some authors have masked clouds reasonably well (e.g. Gesell, 1989; Raschke and others, 1992; Baum and Trepte, 1999) using the reflective and thermal differences that often, but not always, exist between clouds and snow surfaces. Here we make use of the reflective and thermal differences in AVHRR channel 3 ($3.55\text{--}3.93\ \mu\text{m}$) and the thermal differences in channel 4 ($10.5\text{--}11.5\ \mu\text{m}$) that are often present. We empirically found that the following normalized differential index masks most clouds over Vatnajökull:

$$R_{34} = \frac{C_3 - C_4}{C_3 + C_4}, \quad (1)$$

where C_i is the raw count level in AVHRR channel i . Depending on the temperature difference with the surface, clouds are mostly discernible from the surface in one or both of these

channels. Therefore, R_{34} often detects clouds in different thermal ranges, over snow and ice and over bare land as well. For each individual image, we apply a threshold for R_{34} to mask clouds. This method does not detect all clouds, so we had to check the images manually for errors. A convenient way of doing this is to compare subsequent images and look at textural characteristics. On some images, a difference between the detected cloud margin and the corresponding change in albedo is present, which is caused by shadow casting. However, this applies only to few images and to small areas. As an example we show channel 1 (operating in the visible part of the spectrum) count number and R_{34} for one image (Fig. 4). In the west, bright clouds, obscuring the firn line and the ice-cap margin, are visible over the otherwise dark land surface (Fig. 4a). These clouds are visible in a plot of R_{34} , even over snow and ice (Fig. 4b).

3.2. Geolocation

We apply a geolocation to each image by comparing the images to the DEM. The horizontal resolution of the DEM is smaller than the AVHRR pixel size, namely, 500 m. The DEM is given in rectangular coordinates, while the AVHRR images are given in cylindrical stereographic coordinates. Because of this we have to rotate the images slightly around the centre of the ice cap in order to obtain a good fit. Then we fit the ice-cap margin and several height contours from the DEM to AVHRR channels 1 and 3. Channel 1 shows sharp mountain peaks and steep ridges (because of changes in surface albedo), and channel 3 clearly shows the margin of the ice cap (because melting snow and ice, unless heavily debris-covered, are colder than land). We were able to locate these features on most images with an accuracy of one pixel. The accuracy of the geolocation for a few images with a large satellite viewing angle is estimated to be two pixels.

3.3. Calibration

The AVHRR instruments record radiation intensities, which must be converted into radiances. Rao and Chen (1995, 1999) provide calibration coefficients for channels 1 and 2 of the AVHRR instruments aboard the NOAA-11 and NOAA-14 satellites, respectively. These coefficients take into account instrument drift. The radiances are simply converted into planetary albedos at the top of the atmosphere by taking into consideration the solar elevation and the distance between the Sun and the Earth.

3.4. Atmospheric correction

The effect of the atmosphere on the albedo is generally linear:

$$\alpha_{\text{surf},i} = a_i + b_i \alpha_{\text{pla},i}, \quad (2)$$

where $\alpha_{\text{surf},i}$ is the surface albedo in channel i , $\alpha_{\text{pla},i}$ is the planetary albedo in channel i , and a_i and b_i are constants for channel i that depend on the surface altitude, the solar zenith angle, the satellite zenith angle and the composition of the atmosphere. For a given image and assuming a horizontally homogeneous atmosphere over the ice cap, the constants are only a function of surface altitude (Reijmer, 1997). This means that we only have to calculate this dependence once for each entire image. The atmospheric correction can then simply be applied to all image pixels, because the DEM gives us the altitude of the surface in a pixel. The constants are calculated by means of a radiative transfer model (Koelemeijer and others, 1993) which is based on the model of Slingo and Schrecker

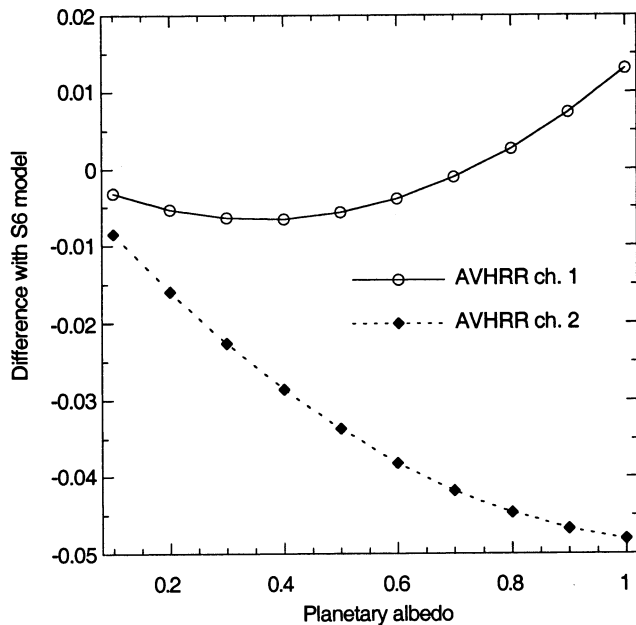


Fig. 5. Difference between the surface albedo from the 6S radiative transfer model and from the Slingo and Schrecker (1982) model as a function of planetary albedo. For both models, the same solar zenith angle (about 50°), surface elevation (250 m) and atmospheric profile were used. The zenith angles are representative of the images used in this paper. Differences are shown for the AVHRR channels 1 and 2 narrowband albedos.

(1982). It takes into account Rayleigh scattering and attenuation by ozone and water vapour, but neglects the effect of aerosols. The model is physically less complex than models such as the 6S radiative transfer model (Tanre and others, 1992; Fily and others, 1997; Stroeve and others, 1997) but also less time-consuming. When we compare the two models for a representative solar zenith angle and with the same atmospheric profile, the resulting surface narrowband albedos appear to differ very little for AVHRR channel 1, but more for channel 2 (Fig. 5). However, the two differences partially counteract, and, moreover, $\alpha_{\text{srf},1}$ has a much larger weight in the surface broadband albedo than $\alpha_{\text{srf},2}$ (see below). Because of this, the surface broadband albedos of the two models do not differ more than 0.012 for the entire range of albedo values. This comparison is made for a surface altitude of 250 m, so the differences will probably be even smaller for most of Vatnajökull, where the altitude is higher and the atmospheric correction smaller. Therefore, we conclude that it is not necessary to use the more time-consuming 6S model. Because the results of both models are not very sensitive to the atmospheric profiles (Reijmer, 1997; Stroeve and others, 1997), we use the standard Sub Arctic Summer Profile of McClatchey and others (1972) as input.

3.5. Narrow- to broadband conversion

The surface narrowband albedos that are measured in AVHRR channels 1 and 2 have to be converted into a broadband albedo over the solar spectrum. Here we use the empirical expression (personal communication from W. Greuell, 2001)

$$\alpha_{\text{srf}} = 0.508\alpha_{\text{srf},1} + 0.065\alpha_{\text{srf},1}^2 + 0.268\alpha_{\text{srf},2}, \quad (3)$$

where α_{srf} is the surface broadband albedo. This expression is based on many (8000) point measurements that were made simultaneously in AVHRR channels 1 and 2 and over the entire solar spectrum. Incoming fluxes were measured

on the ice-cap surface, and outgoing fluxes were measured from a helicopter that flew at low altitude over Vatnajökull. Methods and data from this experiment are described in Greuell and others (in press). A broad range of surface types was observed, ranging from dirty glacier ice to melting snow and having broadband albedos between 0.05 and 0.80. Equation (3) corresponds very well to the data, with a residual standard deviation of 0.008. Measurements over dry snow are not available, but during the melting season dry snow hardly occurs on Vatnajökull.

3.6. Anisotropic correction

Snow and ice reflect solar radiation anisotropically, so the satellite-derived albedo depends on the view geometry. The function that describes the reflection of solar radiation as a function of the view geometry is called a bidirectional reflectance distribution function (BRDF). It varies with wavelength, solar elevation and (sub)surface properties such as grain-size and impurity content (e.g. Warren, 1982; Nolin and Stroeve, 1997). Liquid water has an indirect effect because it enlarges the effective grain-size. Although existing theoretical models take these effects into account (e.g. Fily and others, 1997; Nolin and Stroeve, 1997; Leroux and others, 1998), it is not (yet) possible to extract independent information about grain-size, water content and impurity content from satellite imagery. We use an empirical BRDF (Koks, 2001) that is based on measurements above melting snow 2 or 3 weeks old and is valid for a broad range of solar zenith angles (15.9 – 65.5°). The methods and derivation of this BRDF are nearly the same as in Greuell and De Ruyter de Wildt (1999). The measurements were made in Landsat Thematic Mapper (TM) bands 2 and 4, but following Greuell and De Ruyter de Wildt (1999) we can argue that they are also applicable to AVHRR bands 1 and 2, respectively. During the summer, virtually all surface snow of Vatnajökull is melting and metamorphosed, so the parameterization is likely to be valid for the average summer conditions on Vatnajökull. The parameterization is given in the Appendix.

Greuell and De Ruyter de Wildt (1999) present empirical BRDFs that were measured over ice on Morteratschgletscher, Switzerland. It is, however, questionable whether these are applicable to Vatnajökull. Glacier ice may contain air bubbles, dust inclusions and cracks that influence anisotropy. Moreover, much of the glacier ice of northern Vatnajökull (Dyngjujökull and large parts of Brúar- and Köldukvíslarjökull; see Fig. 6) is partly or entirely covered by volcanic deposits, called tephra, which reflect solar radiation more isotropically than snow and ice. For these reasons we did not apply any corrections for anisotropy over glacier ice and tephra-covered glacier ice.

3.7. Correction for surface inclination

In the above, the fluxes are calculated with respect to a horizontal plane. This means that over a horizontal surface the calculated albedo is the actual surface albedo. However, if the surface is inclined, the fluxes through a plane parallel to the surface differ from those through the horizontal plane, and a correction needs to be applied to obtain the surface albedo. We calculate the surface albedo with the expression of Knap and others (1999). This expression is only valid for isotropic reflection, so we only apply it over glacier ice. Over snow surfaces, the surface inclination is taken into account by applying the correction for anisotropy with respect to the inclined surface.

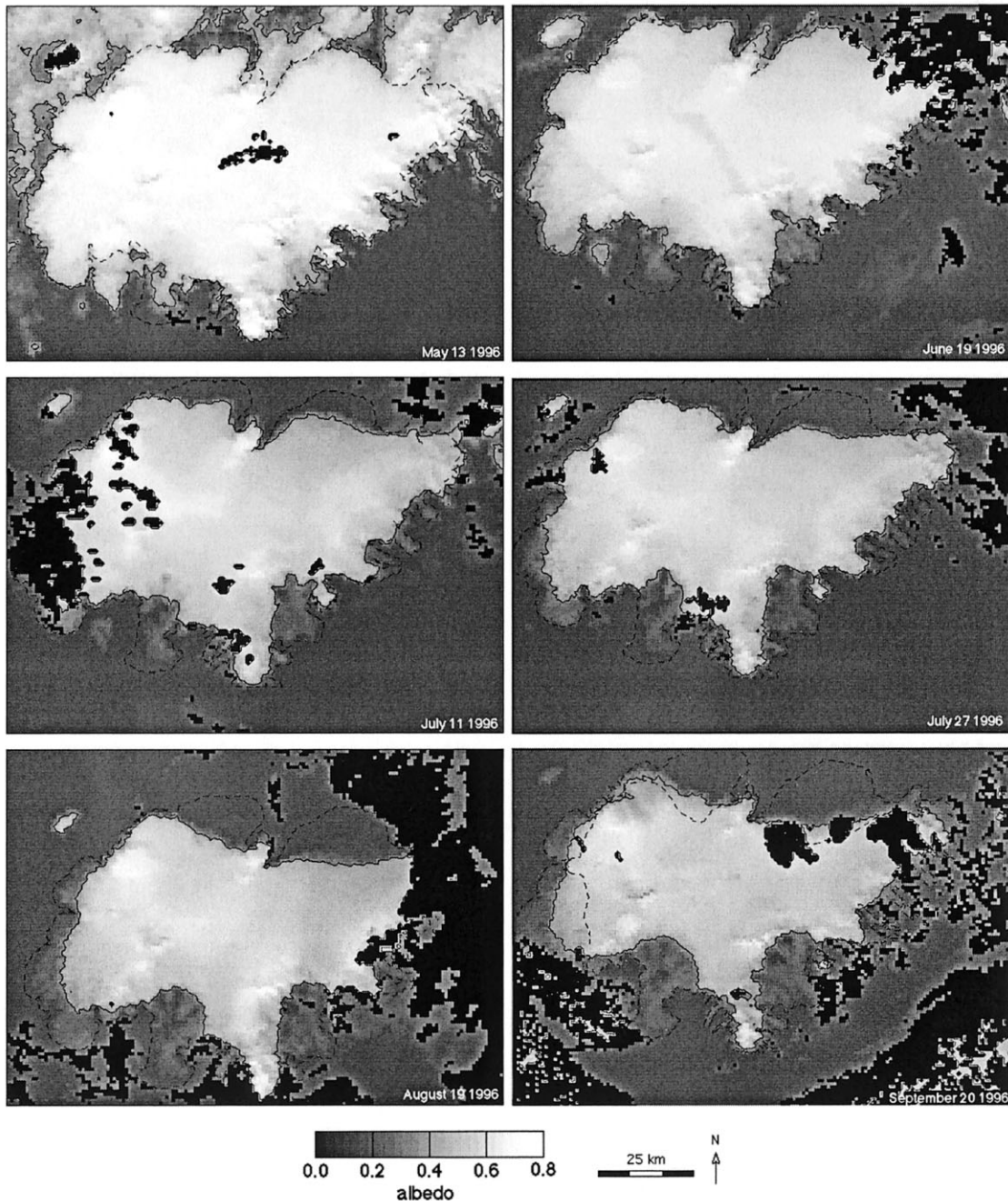


Fig. 6. Six selected NOAA AVHRR albedo images for summer 1996. Each image shows the margin of Vatnajökull (dashed line) and the 0.35 albedo contour (solid line). In the last image (20 September), the equilibrium line is also plotted (inner dashed line). The equilibrium line is obtained by interpolating the mass-balance measurements, as described in the text. Because the mass balance was only measured over the northwestern half of Vatnajökull, no equilibrium line is plotted in the south and southeast.

4. SATELLITE IMAGES: RESULTS

4.1. Development of the surface albedo during the summer

Figure 6 displays some images with few clouds of the summer of 1996. The images show a gradual decrease of the albedo in the accumulation area, from about 0.8 to about 0.6, and a gradual rise of the snowline. In August this rise comes to a standstill, and the situation remains stationary until the end of the melting season. This is probably a consequence of the albedo of firn being close to the albedo of relatively old snow. The albedo is more constant in time in the ablation area than in the accumulation area. In the northern and northwestern ablation areas, the albedo is very low (around 0.1) and quite homogeneous, due to the tephra covering the ice in this region. Zones with clean ice do occur (Larsen and others,

1998), but they are not resolved by the AVHRR images. In the south and southeast, the albedo of the ablation area varies considerably on the satellite pixel scale and lies between 0.15 and 0.35 (Fig. 6). On a smaller scale there is even more variability in these regions (Reijmer, 1997).

4.2. Errors

All processing steps introduce some uncertainty in the surface albedo. The uncertainties resulting from most processing steps are not very large: less than 0.05 (Reijmer, 1997). The uncertainty introduced by neglect of anisotropy over ice and by the correction for anisotropy over snow is hard to quantify. It will be largest for large satellite zenith angles and extreme surface types (either extremely wet and metamorphosed snow or dry snow). From the information available about BRDFs (e.g. Suttles and others, 1988; Stroevé and

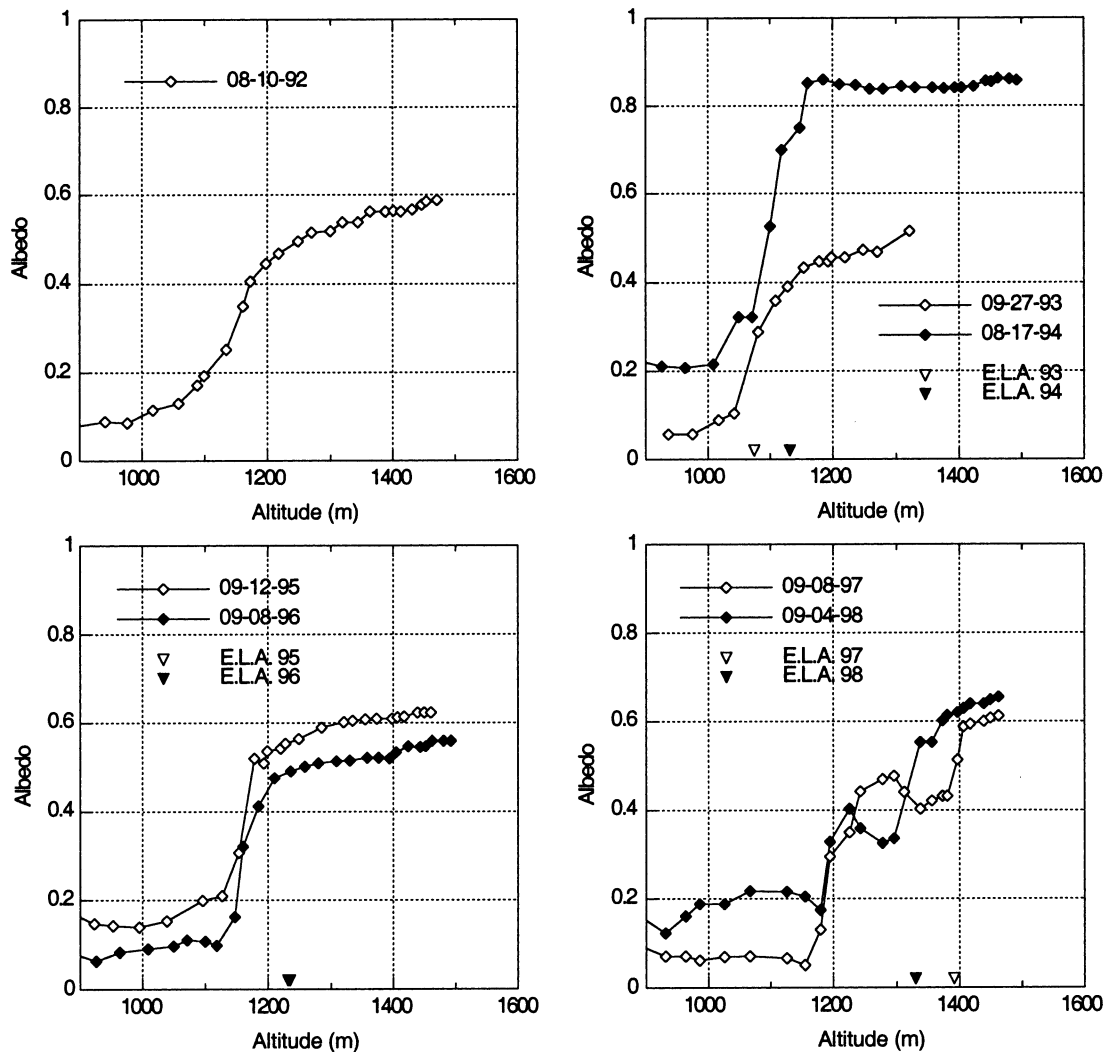


Fig. 7. Satellite-derived albedo profiles along a flowline of western Brúarjökull at the end of the melting season, for several years. The mass-balance measurements from which the ELAs are determined were made along the same flowlines. In 1992, no measurements were made on Brúarjökull, and no suitable image is available for the end of the 1999 melting season. The ELA in 1995 was the same as in 1996. For all years, the image that displays the highest firn line is used to obtain the profiles. Dates: mm-dd-yy.

others, 1997; Greuell and De Ruyter de Wildt, 1999) we estimate the uncertainty to be 0.15 in extreme cases but considerably smaller for most images and locations.

5. MASS-BALANCE RETRIEVAL FROM SATELLITE IMAGES

5.1. Detection of firn line and equilibrium line

According to Østrem (1975), it may be possible to infer B from satellite images if the equilibrium line can be detected. This idea is based on the linear relation between the ELA and B . We investigate this for two representative outlets of Vatnajökull, namely, Brúarjökull in the northeast and Tungnaárjökull in the west. Figures 7 and 8 display albedo profiles of these two outlets at the end of several melting seasons. Note that there are no profiles for 1999, due to a lack of cloud-free images at the end of the summer. Over Brúarjökull the transition from ice to firn and snow is quite sharp in most years, but over Tungnaárjökull it is often too gradual to be determined accurately. The annual mass-balance measurements on Tungnaárjökull display strong fluctuations superimposed upon a linear increase with altitude, probably caused by snow-drift. Synthetic aperture radar images from the European Space Agency ERS satellites with a horizontal resolution of

33 m (not shown here) show that there is no real firn line on Tungnaárjökull, but rather a transition that occurs in patches. This can partially be seen in the profile over Tungnaárjökull for 1993 (Fig. 8), but mostly the resolution of the AVHRR images is too low to resolve the patches. Both on Brúarjökull and on Tungnaárjökull the transition coincides with the equilibrium line in 1993 and 1994, which were years with a positive B (Table 1). In 1995–98, which were all years with a negative B , the equilibrium line lay significantly higher than the upper ice margin, which means that firn had emerged at the surface. It is also interesting to see that on both outlets the firn line was located at approximately the same altitude in these 4 years (Figs 7 and 8). In consecutive years of negative B the firn line will rise, of course, but only very slowly. The firn line therefore marks a transition between nearly static glacier facies (the wet-snow zone and the ablation area), which is the result of meteorological processes during the last years or decades. Hence, the firn line reflects the mean equilibrium line over several years. The same has been observed by Hall and others (1995) and König and others (2001), who found that the firn line coincides with a radar backscatter boundary related to subsurface glacier facies. On Brúarjökull a second transition was present in 1997 and 1998, the years with the highest equilibrium line (Fig. 7). This second transition coincides with the equilibrium line and we assume that

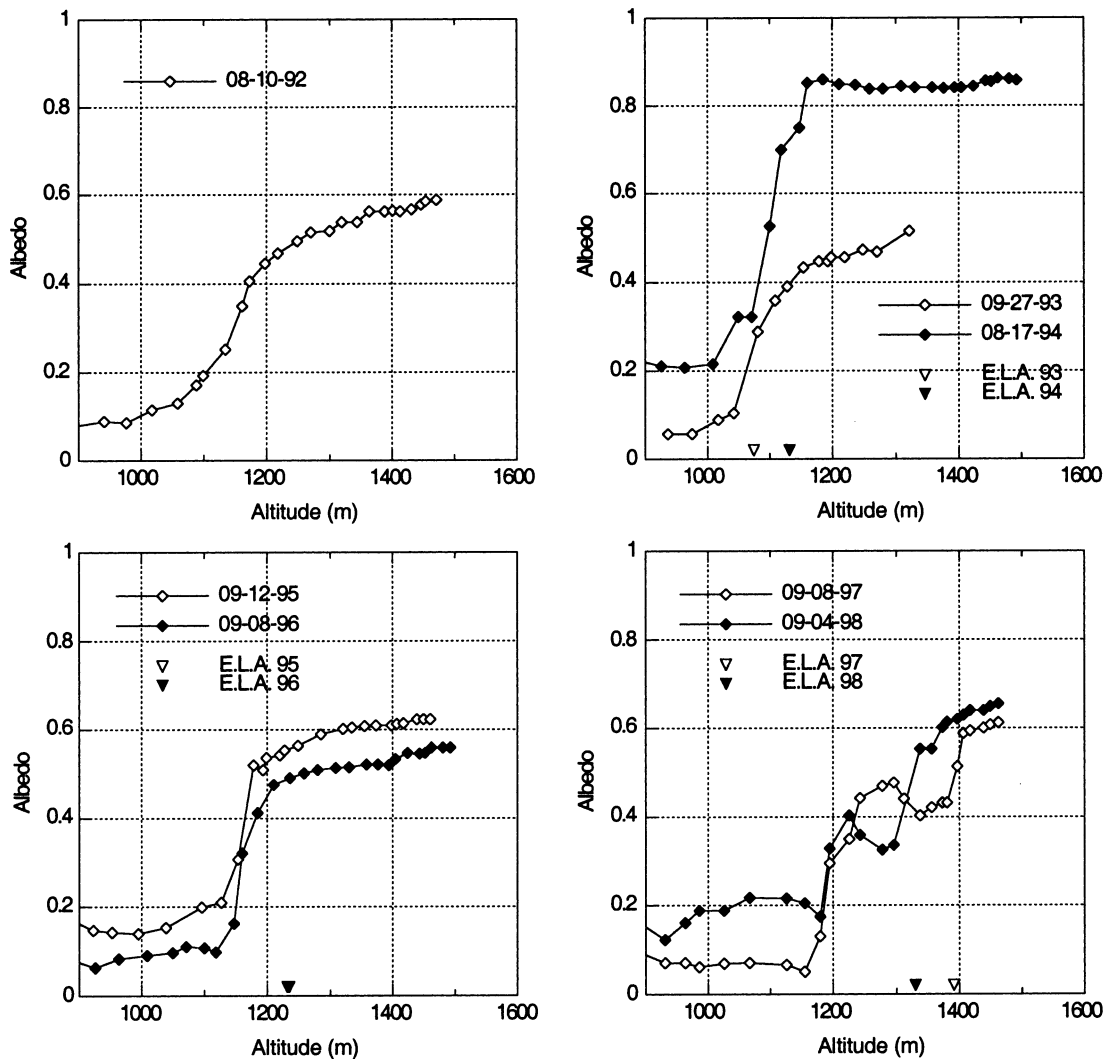


Fig. 8. Satellite-derived albedo profiles along a flowline of Tungnaárjökull at the end of the melting season, for several years. The mass-balance measurements from which the ELAs are determined were made along the same flowlines. In 1995 and 1996, no measurements were made on Tungnaárjökull, and no suitable image is available for the end of the 1999 melting season. For all years, the image that displays the highest firn line is used to obtain the profiles. Dates: mm-dd-yy.

it is the boundary between the snow and firn. However, this higher transition did not occur in all years and not on Tungnaárjökull, so it cannot be used to determine the equilibrium line. Summarizing, the equilibrium line is detectable on satellite albedo images when it is not located above its position of the previous year(s), i.e. the firn line. In years when the snow-line retreats far enough to reveal firn, albedo monitoring is of limited use for determining the equilibrium line because of the small albedo difference between snow and firn.

5.2. Mass-balance retrieval from the integrated surface albedo

The appearance of firn and/or slush with low albedos in warm years obscures the equilibrium line, but at the same time provides extra information that may be used to infer *B*. For example, the mean albedo of the entire accumulation area depends on the age of the snow and hence on the mass balance in the accumulation area. The mean surface albedo of the ice cap not only reflects the amount of accumulation and ablation in the preceding part of the mass-balance year but also strongly affects net shortwave radiation and hence summer melt. To take this feedback into account, we convert

the satellite-derived surface albedo into the net potential global radiation:

$$Q_{\text{pot,net}} = Q_{\text{pot}}(1 - \alpha_{\text{srf}}), \tag{4}$$

where α_{srf} is the satellite-derived surface albedo, Q_{pot} is the potential global radiation, defined as the incoming solar radiation at the top of the atmosphere, and $Q_{\text{pot,net}}$ is the net potential global radiation. $Q_{\text{pot,net}}$ is the potential absorption of solar energy per unit surface area. This differs from the actual absorption of solar energy (Q_{net}) which is lower due to atmospheric attenuation. However, the satellite images mostly display low cloudiness or no cloudiness at all and are in this respect not representative. Cloudiness strongly determines the amount of solar energy that reaches the surface, but the average cloudiness over a time interval is not known over remote and/or large ice caps and glaciers. Hence it is not possible to retrieve Q_{net} over long time intervals from satellite images, which is why we compute $Q_{\text{pot,net}}$ instead. Note that it is necessary to take into account atmospheric effects upon the albedo, because several processing steps in the albedo retrieval process need to be applied upon the surface albedo, and not upon the planetary albedo (e.g. anisotropic correction, narrow- to broadband conversion).

Q_{pot} is easily calculated from standard astronomical

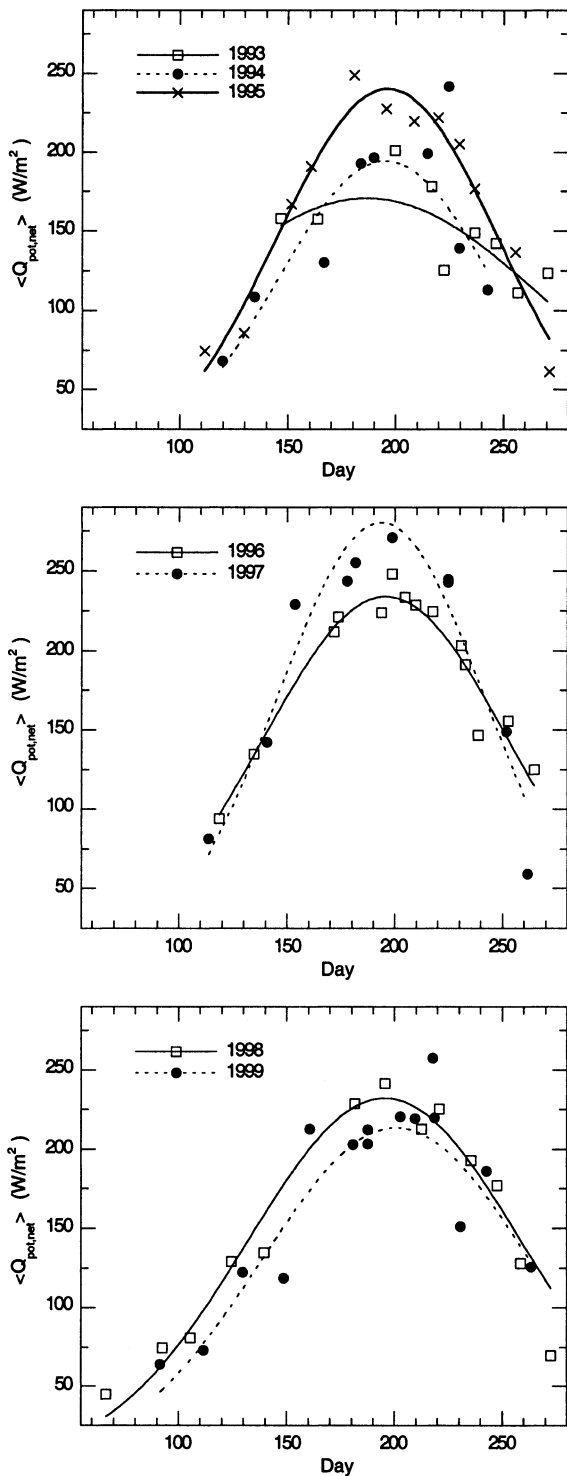


Fig. 9. Satellite-derived net potential global radiation ($\langle Q_{pot,net} \rangle$), averaged over the northwestern part of Vatnajökull, as a function of the day of the year. Data for several years are shown. The curves are fits of Equation (6) to the data points.

theory (e.g. Walraven, 1978). We propose that $Q_{pot,net}$, integrated over the ice cap and over the summer, is related to B :

$$B \propto \sum_{\text{summer}} \langle Q_{pot,net} \rangle = \sum_{\text{summer}} \frac{1}{A} \sum_{\text{glacier}} Q_{pot,net}, \quad (5)$$

where $\langle Q_{pot,net} \rangle$ is the net potential global radiation, averaged over the surface with area A . Equation (5) can be evaluated by simple linear interpolation between the days for which images are available, but this may result in unrealistic curves when few images are available. Also, all images from which $\langle Q_{pot,net} \rangle$ is derived may show partial cloud cover, and the visible part of a drainage basin may not be represen-

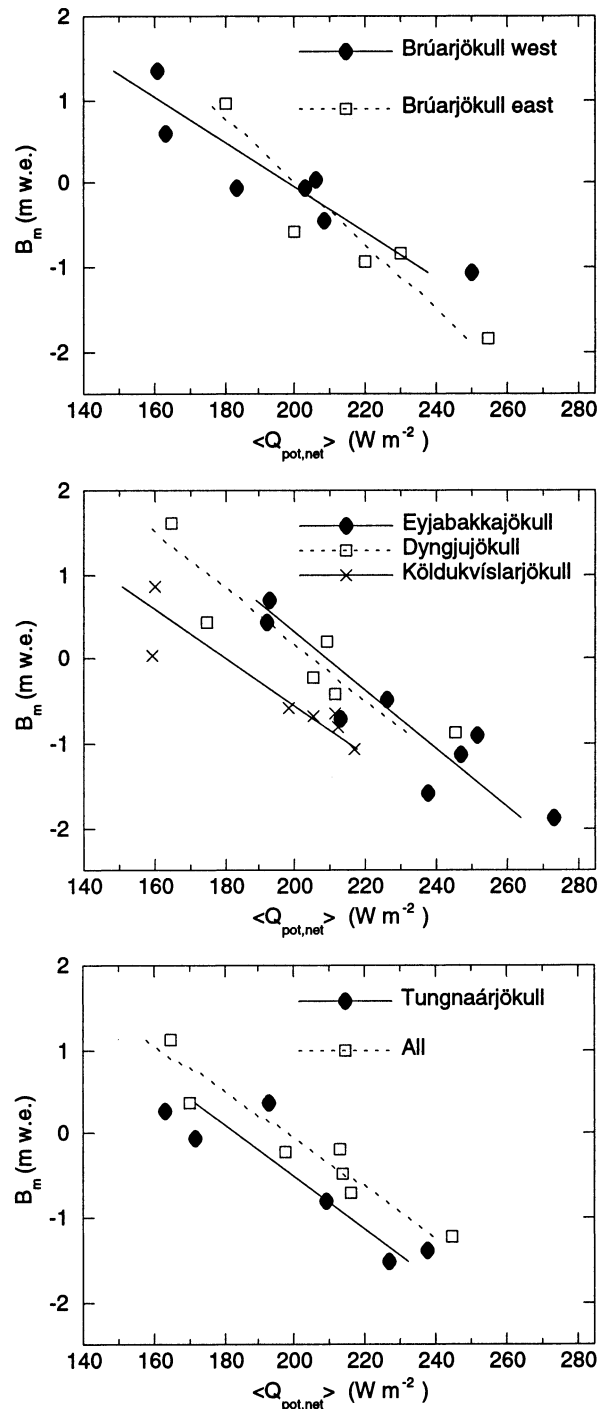


Fig. 10. $\langle Q_{pot,net} \rangle$ integrated over part of the melting season (days 146–242), as a function of the specific balance. The average $\langle Q_{pot,net} \rangle$ per day during the integration period is shown. “All” indicates the entire area where mass-balance measurements were taken (i.e. all mentioned drainage basins).

tative of the entire drainage basin. Therefore, we use an analytical expression for $\langle Q_{pot,net} \rangle$ that incorporates a priori knowledge about the course of $\langle Q_{pot,net} \rangle$ during the summer. We find that the following function fits well to the data (disregarding disturbances by clouds):

$$\langle Q_{pot,net} \rangle = a \exp \left[-\frac{(\text{day} - b)^2}{c} \right], \quad (6)$$

where day is the day of the year, and a , b and c are constants. This function resembles a normal distribution and has a maximum magnitude a at day b and approaches zero on either side of this maximum. The constant c indicates the

width of the curve. We fit this expression to the satellite-derived values of $\langle Q_{\text{pot,net}} \rangle$, which are weighted with the percentage of glacier area that is visible. This means that images with few clouds have large weights, and images with many clouds have small weights. As an example we show fits of Equation (6) to the satellite-derived values of $\langle Q_{\text{pot,net}} \rangle$ for the entire northwest of Vatnajökull (Fig. 9). Deviations from the curve fits are mainly caused by clouds (these data points have small weights) and snowfalls. For example, the high value of $\langle Q_{\text{pot,net}} \rangle$ on day 224 in 1994 is caused by clouds (84% of the satellite pixels are classified as clouds). The low value of $\langle Q_{\text{pot,net}} \rangle$ on day 238 in 1996 is caused by high albedos due to recent snowfall. On the image taken at this day, the snowline lies well below the firn line during the weeks before and after this day.

When we use a time-step of 1 day and integrate Equation (6) over the longest period covered by the satellite images in all years (days 146–242), we find that the integrated values of $\langle Q_{\text{pot,net}} \rangle$ correlate linearly with B (Fig. 10). Prescribing fewer degrees of freedom by setting b and/or c to some value or by using second- and third-order polynomials instead of Equation (6) hardly affects this. When we consider only the albedo instead of $Q_{\text{pot,net}}$ the results do not improve either and even become slightly worse, probably because the total amount of solar energy delivered to the surface is disregarded. For all drainage basins the correlation between $\langle Q_{\text{pot,net}} \rangle$ and B is high (Table 2).

6. DISCUSSION

The methods that lead to the data in Figure 10 all introduce some uncertainty, which must be taken into account to assess the applicability of the $B - \langle Q_{\text{pot,net}} \rangle$ regression model. The uncertainty in the directly measured B is difficult to assess, and for all drainage basins we will use the same first-order estimate. From comparing different estimates of B we estimate the uncertainty to be 0.25 m w.e., which is a conservative value. The uncertainty due to the regression model ranges from 0.24 m w.e. (the entire northwest of Vatnajökull) to 0.51 m w.e. (Tungnaárjökull). The largest uncertainty is introduced by $\langle Q_{\text{pot,net}} \rangle$ (Table 2). The source of this uncertainty is two-fold: the satellite-retrieval method introduces an uncertainty, and there is an error associated with the analytical expression for $Q_{\text{pot,net}}$ (Fig. 9). The resulting error in the satellite-retrieved specific mass balance (B_{sat}) is computed from the regression

coefficient $dB/d\langle Q_{\text{pot,net}} \rangle$. This slope, and hence the resulting error in B_{sat} , tends to increase with precipitation. The total error in B_{sat} ranges from 0.50 m w.e. (Köldukvíslarjökull) to 0.76 m w.e. (eastern Brúarjökull), which is 2–3 times as large as the error in the direct observations of B . It is interesting to note that, just like the error in B_{sat} , the overall range of annual mass balance tends to increase with mean annual precipitation. This range is 1.8–2.8 m w.e. for different parts of Vatnajökull (Fig. 10). The result is that for all drainage basins the ratio between the error in B_{sat} and the range of annual mass balance is nearly the same, namely, $27 \pm 3\%$. Hence, for all drainage basins of Vatnajökull, the satellite retrieval method can only positively detect annual changes in B that are larger than $27 \pm 3\%$ of the range of annual mass balance.

The larger uncertainty in B_{sat} also has implications for the possibility of estimating trends and averages. For example, the average B (Table 1) only differs significantly from zero (at the 95% confidence level) for Eyjabakkajökull. For all other drainage basins, more annual measurements than presently available are required to make such a statement. The number of annual measurements needed for this statement (n_y) increases when the error in the mass-balance measurement increases, as is the case when the satellite retrieval method is used. The observed variance in B is partly due to natural variability and partly due to the measurement error in B . When we replace the measurement error in B with the error in B_{sat} , we find that for all drainage basins n_y becomes about 50% larger.

7. CONCLUSIONS

Remote-sensing instruments are useful tools for observing glaciers and ice caps without the need to actually go there. The most obvious feature on the surface of glaciers and ice caps is the transition from ice to firn or snow, which can be successfully observed. However, this boundary is not always equal to the equilibrium line and hence not always related to the mass balance. This is often the case when the equilibrium line is located above its position of the previous year(s), because then firn is exposed, which obscures the equilibrium line. Very small differences in albedo and texture between snow and firn make the equilibrium line hard, if not impossible, to detect in these years. This is especially true when no a priori information is available and one does not know where to expect the equilibrium line. Occasion-

Table 2. Statistics for the linear $B - \langle Q_{\text{pot,net}} \rangle$ regression model. The mean annual precipitation for each drainage basin is also shown. “All” indicates the entire area where mass-balance measurements were taken (i.e. all mentioned drainage basins)

Drainage basin	Correlation coefficient	Explained variance	Error in B m w.e.	Error due to regression model m w.e.	Error in $\langle Q_{\text{pot,net}} \rangle$ m w.e.	Total error m w.e.	Annual precipitation m
Western Brúarjökull	0.89	0.8	0.25	0.34	0.42	0.59	2.7
Eastern Brúarjökull	0.94	0.87	0.25	0.34	0.63	0.76	2.9
Eyjabakkajökull	0.9	0.81	0.25	0.39	0.55	0.72	3.2
Dyngjufjökull	0.9	0.81	0.25	0.37	0.51	0.68	2.4
Köldukvíslarjökull	0.92	0.85	0.25	0.25	0.35	0.5	2.1
Tungnaárjökull	0.87	0.76	0.25	0.51	0.46	0.73	2.3
All	0.95	0.91	0.25	0.24	0.47	0.59	2.7

Note: The error in $\langle Q_{\text{pot,net}} \rangle$ is for each drainage basin averaged over the years, because the error associated with the analytical expression for $\langle Q_{\text{pot,net}} \rangle$ differs from year to year.

ally, the equilibrium line is visible as a secondary jump in albedo, but this is not the case in all years with a negative B and not on all outlets. Apart from these problems, the ice–snow transition is not always sharp and, depending upon glacier size and climatic setting, satellite and DEM resolution may limit the possibility of inferring changes in ELA from satellite imagery (Demuth and Pietroniro, 1999). In one year there were too many clouds to find a suitable image of the end of the melting season.

These problems are not encountered when one studies the mean surface albedo of the entire drainage basin during the melting season, and not merely a boundary between two facies on a certain day. In years with a negative B , much relatively dark firn is present, while little summer snowfall and high melt rates may also contribute to a darkening of the surface. In years with a positive B , no firn is exposed, more glacier ice is covered by snow, and summer snowfall may brighten the surface. The albedo feedback (which strengthens the correlation between B and the albedo) is taken into account by weighting the mean surface albedo with the potential global radiation so that the mean net potential global radiation ($\langle Q_{\text{pot,net}} \rangle$) is obtained. By using $Q_{\text{pot,net}}$, and not the global radiation at the surface, one does not need to know the average cloudiness. Consequently, the method can be applied easily to any ice cap and glacier in the world by using satellite data alone. $\langle Q_{\text{pot,net}} \rangle$ is strongly related to surface melt and also depends on winter precipitation and melt earlier in the melting season. Because $\langle Q_{\text{pot,net}} \rangle$ varies during the summer, the surface during the whole summer must be studied in order to extract all available information. An additional advantage of studying several images is that one does not need to find one cloud-free image of the end of the summer that is not disturbed by snowfall. We find that $\langle Q_{\text{pot,net}} \rangle$, integrated over the melting season, is linearly related to B . Due to uncertainties in measurements and methods, this relation can only be used to detect changes in B of at least 0.50–0.76 m w.e. (for different parts of Vatnajökull). This is two to three times larger than the uncertainty in the directly measured B , which implies that more annual measurements are required in order to confidently estimate averages and trends when the satellite retrieval method is used.

The linear relations between B and $Q_{\text{pot,net}}$ are based upon data from years with very positive and with very negative values of B . The drainage basins for which these relations are found have different hypsometries, climate settings (different amounts of precipitation) and states of mean balance. Therefore, we expect that yearly variations in B of any ice cap or glacier can be estimated qualitatively with the method presented in this paper. The exact magnitude of yearly variations can only be deduced if the slope of the linear relation is known, and the value of B only if both slope and offset are known. Therefore, the method can be used to estimate B quantitatively for (parts of) Vatnajökull. Note, however, that there is no theoretical ground for the relation between the net potential global radiation and B to be linear for all ice masses. It would be interesting to deduce this relationship for (part of) the Greenland ice sheet (with superimposed-ice and slush zones) and for alpine glaciers (with steeper and more varying slopes). Unfortunately, NOAA images can only be used for ice sheets and ice caps of considerable size. For alpine glaciers images from satellites with a higher resolution (e.g. Landsat) must be used, but these are much less frequently available and are more expensive. This means that

the method presented in this work is most suitable for fairly large ice caps and glaciers.

ACKNOWLEDGEMENTS

We thank W. Greuell for sharing his expertise in image processing and giving useful advice. We also thank A. Brooks and N. Lonie of the Satellite Receiving Station in Dundee for their technical support, selection of images, and patience when we failed to download the images properly. We are also grateful to O. Sigurðsson, two anonymous reviewers and the scientific editor H. Rott for useful comments upon the manuscript. O. Sigurðsson kindly provided mass-balance data for Eyjabakkajökull. C. H. Reijmer purchased some of the AVHRR images. This work was funded by SRON (Foundation for Space Research, the Netherlands), project No. co-030.

REFERENCES

- Abdalati, W. and K. Steffen. 1998. Accumulation and hoar effects on microwave emission on the Greenland ice-sheet dry-snow zones. *J. Glaciol.*, **44**(148), 523–531.
- Adam, S., A. Pietroniro and M. M. Brugman. 1997. Glacier snow line mapping using ERS-1 SAR imagery. *Remote Sensing Environ.*, **61**(1), 46–54.
- Baum, A.A. and Q. Trepte. 1999. A grouped threshold approach for scene identification in AVHRR imagery. *J. Atmos. Oceanic Technol.*, **16**, 793–800.
- Björnsson, H., F. Pálsson, M. T. Guðmundsson and H. H. Haraldsson. 1997. *Afkoma, Hreyfing og afrennsli á vestan- og norðanverðum Vatnajökli jökuláridi 1995–1996*. Reykjavík, University of Iceland. Science Institute. (Report RH-24-97).
- Björnsson, H., F. Pálsson, M. T. Guðmundsson and H. H. Haraldsson. 1998a. *Mass balance and meteorological observations on Vatnajökull 1997*. Reykjavík, University of Iceland. Science Institute. (Report RH-03-98).
- Björnsson, H., F. Pálsson, M. T. Guðmundsson and H. H. Haraldsson. 1998b. *Mass balance and meteorological observations on Vatnajökull 1998*. Reykjavík, University of Iceland. Science Institute. (Report RH-14-98).
- Björnsson, H., F. Pálsson, M. T. Guðmundsson and H. H. Haraldsson. 1998c. Mass balance of western and northern Vatnajökull, Iceland, 1991–1995. *Jökull*, **45**, 35–58.
- Björnsson, H., F. Pálsson, M. T. Guðmundsson and H. H. Haraldsson. 1999. *Mass balance and meteorological observations on Vatnajökull 1999*. Reykjavík, University of Iceland. Science Institute. (Report RH-24-99).
- Brown, I. A., M. P. Kirkbride and R. A. Vaughan. 1999. Find the firn line: The suitability of ERS-1 and ERS-2 SAR data for the analysis of glacier facies on Icelandic icecaps. *Int. J. Remote Sensing*, **20**(15–16), 3217–3230.
- Demuth, M. and A. Pietroniro. 1999. Inferring glacier mass balance using RADARSAT: results from Peyto Glacier, Canada. *Geogr. Ann.*, **81A**(4), 521–540.
- Ebert, E. 1987. A pattern recognition technique for distinguishing surface and cloud types in the polar regions. *J. Climate Appl. Meteorol.*, **26**(10), 1412–1427.
- Fily, M., B. Bourdelles, J.-P. Dedieu and C. Sergent. 1997. Comparison of *in situ* and Landsat thematic mapper derived snow grain characteristics in the Alps. *Remote Sensing Environ.*, **59**(3), 452–460.
- Gesell, G. 1989. An algorithm for snow and ice detection using AVHRR data: an extension to the APOLLO software package. *Int. J. Remote Sensing*, **8**(4–5), 897–905.
- Greuell, W. and M. S. de Ruyter de Wildt. 1999. Anisotropic reflection of melting glacier ice: measurements and parameterizations. *Remote Sensing Environ.*, **70**(3), 265–277.
- Greuell, W. and W. H. Knap. 2000. Remote sensing of the albedo and detection of the slush line on the Greenland ice sheet. *J. Geophys. Res.*, **105**(D12), 15,567–15,576.
- Greuell, W., C. H. Reijmer and J. Oerlemans. In press. Narrowband-to-broadband albedo conversion for glacier ice and snow based on aircraft and near-surface measurements. *Remote Sensing Environ.*
- Hagen, J. O. and O. Liestøl. 1990. Long-term glacier mass-balance investigations in Svalbard, 1950–88. *Ann. Glaciol.*, **14**, 102–106.
- Hall, D. K., R. S. Williams, Jr and K. J. Bayr. 1992. Glacier recession in Iceland and Austria as observed from space. *Eos*, **73**(12), 129, 135, 141.
- Hall, D. K., R. S. Williams, Jr and O. Sigurðsson. 1995. Glaciological observations of Brúarjökull, Iceland, using synthetic aperture radar and thematic mapper satellite data. *Ann. Glaciol.*, **21**, 271–276.
- Hall, D. K., R. S. Williams, Jr, J. S. Barton, O. Sigurðsson, L. C. Smith and

- J. B. Garvin. 2000. Evaluation of remote-sensing techniques to measure decadal-scale changes of Hofsjökull ice cap, Iceland. *J. Glaciol.*, **46**(154), 375–388.
- Hastenrath, S. and L. Greischar. 1997. Glacier recession on Kilimanjaro, East Africa, 1912–89. *J. Glaciol.*, **43**(145), 455–459.
- Knap, W. H., B. W. Brock, J. Oerlemans and I. C. Willis. 1999. Comparison of Landsat TM-derived and ground-based albedos of Haut Glacier d'Arolla, Switzerland. *Int. J. Remote Sensing*, **20**(17), 3293–3310.
- Koelmeijer, R., J. Oerlemans and S. Tjemkes. 1993. Surface reflectance of Hintereisferner, Austria, from Landsat 5 TM imagery. *Ann. Glaciol.*, **17**, 17–22.
- Koks, M. 2001. Anisotropic reflection of radiation by melting snow. Landsat TM bands 2 and 4. (M.Sc. thesis, Universiteit Utrecht. Instituut voor Marien en Atmosferisch Onderzoek Utrecht (IMAU))
- König, M., J.-G. Winther, N. T. Knudsen and T. Guneriusen. 2001. Firn-line detection on Austre Okstindbreen, Norway, with airborne multi-polarization SAR. *J. Glaciol.*, **47**(157), 251–257.
- Kulkarni, A. V. 1992. Mass balance of Himalayan glaciers using AAR and ELA methods. *J. Glaciol.*, **38**(128), 101–104.
- Larsen, G., M. T. Gudmundsson and H. Björnsson. 1998. Eight centuries of periodic volcanism at the center of the Iceland hot spot revealed by glacier tephrostratigraphy. *Geology*, **26**(10), 943–946.
- Leroux, C., J. Lenoble, G. Brogniez, J. W. Hovenier and J. F. de Haan. 1998. A model for the bidirectional polarized reflectance of snow. *J. Quant. Spectrosc. Radiat. Transfer*, **61**(3), 273–285.
- McClatchey, R. A., R. W. Fenn, J. E. A. Selby and J. S. Garing. 1972. *Optical properties of the atmosphere. Vol. D12. 3rd edition.* Hanscom AFB, MA, Air Force Cambridge Research Laboratory. (AFCRL Rep. 72-0497, Environ. Res. Pap. 411)
- Mote, T. L. and M. R. Anderson. 1995. Variations in snowpack melt on the Greenland ice sheet based on passive-microwave measurements. *J. Glaciol.*, **41**(137), 51–60.
- Nolin, A. W. and J. Stroeve. 1997. The changing albedo of the Greenland ice sheet: implications for climate modeling. *Ann. Glaciol.*, **25**, 51–57.
- Østrem, G. 1975. ERTS data in glaciology — an effort to monitor glacier mass balance from satellite imagery. *J. Glaciol.*, **15**(73), 403–415.
- Pelto, M. S. 1987. Mass balance of south-east Alaska and north-west British Columbia glaciers from 1976 to 1984: methods and results. *Ann. Glaciol.*, **9**, 189–194.
- Rao, C. R. N. and J. Chen. 1995. Inter-satellite calibration linkages for the visible and near-infrared channels of the Advanced Very High Resolution Radiometer on the NOAA-7, -9 and -11 spacecraft. *Int. J. Remote Sensing*, **16**(11), 1931–1942.
- Rao, C. R. N. and J. Chen. 1999. Revised post-launch calibration of the visible and near-infrared channels of the Advanced Very High Resolution Radiometer (AVHRR) on the NOAA-14 spacecraft. *Int. J. Remote Sensing*, **20**(18), 3485–3491.
- Raschke, E., P. Bauer and H. J. Lutz. 1992. Remote sensing of clouds and surface radiation budget over polar regions. *Int. J. Remote Sensing*, **13**(1), 13–22.
- Reijmer, C. H. 1997. *The surface albedo of the Vatnajökull ice cap, Iceland: a comparison between satellite-derived and in situ measurements.* Utrecht, Universiteit Utrecht. Instituut voor Marien en Atmosferisch Onderzoek Utrecht (IMAU). (Internal Report V97-11.)
- Reijmer, C. H., W. H. Knap and J. Oerlemans. 1999. The surface albedo of the Vatnajökull ice cap, Iceland: a comparison between satellite-derived and ground-based measurements. *Boundary-Layer Meteorol.*, **92**(1), 125–144.
- Rott, H. and G. Markl. 1989. Improved snow and glacier monitoring by the Landsat thematic mapper. In *Proceedings of a Workshop on "Earthnet Pilot Project on Landsat Thematic Mapper Applications", held at Frascati, Italy in December 1987.* Noordwijk, Netherlands, European Space Agency, 3–12. (ESA SP-1102)
- Rott, H. and C. Mätzler. 1987. Possibilities and limits of synthetic aperture radar for snow and glacier surveying. *Ann. Glaciol.*, **9**, 195–199.
- Sigurðsson, O. 1999. Jöklabreytingar 1930–1960, 1960–1990 og 1995–1996 / Glacier variations 1930–1960, 1960–1990 and 1995–1996. *Jökull*, **47**, 101–107.
- Slingo, A. and H. M. Schrecker. 1982. On the shortwave radiative properties of stratiform water clouds. *Q. J. R. Meteorol. Soc.*, **108**, 407–426.
- Smith, L. C., R. R. Forster, B. L. Isacks and D. K. Hall. 1997. Seasonal climatic forcing of alpine glaciers revealed with orbital synthetic aperture radar. *J. Glaciol.*, **43**(145), 480–488.
- Steffen, K., W. Abdalati and J. Stroeve. 1993. Climate sensitivity studies of the Greenland ice sheet using satellite AVHRR, SMMR, SSM/I and in situ data. *Meteorol. Atmos. Phys.*, **51**, 239–258.
- Stroeve, J., A. Nolin and K. Steffen. 1997. Comparison of AVHRR-derived and in situ surface albedo over the Greenland ice sheet. *Remote Sensing Environ.*, **62**(3), 262–276.
- Suttles, J. T. and 9 others. 1988. Angular radiation models for Earth-atmosphere system. *U.S. Nat. Aeron. Space Admin. Ref. Publ.* 1184.
- Tanre, D., B. N. Holben and Y. J. Kaufman. 1992. Atmospheric correction algorithm for NOAA-AVHRR products: theory and application. *IEEE Trans. Geosci. Remote Sensing*, **GE-30**(2), 231–250.
- Walraven, R. 1978. Calculating the position of the Sun. *Solar Energy*, **20**(5), 393–397.
- Warren, S. G. 1982. Optical properties of snow. *Rev. Geophys. Space Phys.*, **20**(1), 67–89.
- Williams, R. S., Jr. 1987. Satellite remote sensing of Vatnajökull, Iceland. *Ann. Glaciol.*, **9**, 127–135.
- Williams, R. S., Jr, D. K. Hall, O. Sigurðsson and J. Y. L. Chien. 1997. Comparison of satellite-derived with ground-based measurements of the fluctuations of the margins of Vatnajökull, Iceland, 1973–92. *Ann. Glaciol.*, **24**, 72–80.
- Zwally, H. J. 1977. Microwave emissivity and accumulation rate of polar firn. *J. Glaciol.*, **18**(79), 195–215.

APPENDIX

BRDF OVER MELTING SNOW

For a given surface type and solar zenith angle (θ_s), the bidirectional reflectance (r) that is measured by the satellite sensor only depends upon satellite zenith angle (θ_v) and satellite azimuth angle (φ) (relative to the solar azimuth angle). Bidirectional reflectance is related to surface albedo (α_{srf}) through the anisotropic reflectance factor (f):

$$f(\theta_v, \varphi) = \frac{r(\theta_v, \varphi)}{\alpha_{\text{srf}}} \quad (\text{A1})$$

The parameterization that we use for f over melting snow and firn surfaces reads (Koks, 2001):

$$f(\theta_v, \varphi) = 1 + b_1 \left(\cos \theta_v - \frac{2}{3} \right) + b_2 \theta_v^2 \cos \varphi + b_3 \left(\theta_v \cos^2 \varphi - \frac{\pi}{8} \right) \quad (\text{A2})$$

The derivation of Equation (A2) is nearly the same as in Greuell and De Ruyter de Wildt (1999). The factors b_1 , b_2 and b_3 , which describe the dependence of f upon surface albedo and solar zenith angle, are given by

$$b_i = a_{i,0} + a_{i,1} \alpha + a_{i,2} \theta_s, \quad (\text{A3})$$

where i is 1, 2 or 3 and θ_s must be given in degrees. Values of the coefficients $a_{i,0}$, $a_{i,1}$ and $a_{i,2}$ for Landsat TM bands 2 and 4 are listed in Table 3.

Table 3. Values of the coefficients $a_{i,0}$, $a_{i,1}$ and $a_{i,2}$ in Equation (9). The coefficients are given for Landsat TM bands 2 and 4

i	TM2			TM4		
	$a_{i,0}$	$a_{i,1}$	$a_{i,2}$	$a_{i,0}$	$a_{i,1}$	$a_{i,2}$
1	0.92	-0.735	-0.00661	0.763	-0.619	-0.00776
2	0.1	-0.159	-0.00182	0.133	-0.24	-0.00243
3	-0.157	0.236	0.000404	-0.345	0.598	-0.000388